

# Excluded volume effects in compressed polymer brushes: A density functional theory

Cangyi Chen,<sup>1</sup> Ping Tang,<sup>1,a)</sup> Feng Qiu,<sup>1,a)</sup> and An-Chang Shi<sup>2</sup>

<sup>1</sup>The State Key Laboratory of Molecular Engineering of Polymers, Key Laboratory of Computational Physical Sciences, Department of Macromolecular Science, Fudan University, Shanghai 200433, China

<sup>2</sup>Department of Physics and Astronomy, McMaster University, Hamilton, Ontario L8S 4M1, Canada

(Received 13 January 2015; accepted 12 March 2015; published online 27 March 2015)

A classical density functional theory (DFT) is applied to investigate the behavior of compressed polymer brushes composed of hard-sphere chains. The excluded volume interactions among the chain segments are explicitly treated. Two compression systems are used to study the behavior of brush-wall and brush-brush interactions. For the brush-brush systems, an obvious interpenetration zone has been observed. The extent of the interpenetration depends strongly on the grafting density. Furthermore, the repulsive force between the brush and wall or between the two brushes has been obtained as a function of the compression distance. Compared to the prediction of the analytic self-consistent field theory, such force increases more rapidly in the brush-wall compression with high polymer grafting densities or at higher compressions. In the brush-brush compression system, the interpenetration between the two compressed brushes creates a “softer” interaction. The influence of hard-sphere solvents on the behavior of compressed brushes is also discussed. © 2015 AIP Publishing LLC. [<http://dx.doi.org/10.1063/1.4916133>]

## I. INTRODUCTION

Polymer chains with their ends grafted to a surface provide a crucial model for many important problems in polymer science and biophysics.<sup>1–3</sup> Since the 1970s, this classical system has been extensively studied by numerous groups using different experimental and theoretical methods.<sup>4,5</sup> The properties of end-grafted chains have a strong dependence on the grafting density. At a low grafting density, the grafted chains do not overlap with each other, thus forming conformations resembling isolated “mushrooms”. When the grafting density is high enough to allow overlap between the individual chains, the grafted chains tend to stretch away from the substrate and form stretched conformations.

A simple scaling theory for a polymer brush was first developed by Alexander<sup>6</sup> and de Gennes.<sup>7,8</sup> These authors assumed that the segment density profile is a constant from the grafting surface up to the maximum brush height and the free ends of the chains are strictly located at the outer edge of the brush. Later, the analytic self-consistent field (SCF) theory has been used to investigate the polymer brush density profile and the distribution of the free ends.<sup>9–13</sup> In particular, Milner, Witten, and Cates (MWC) made a significant contribution to a better understanding of the polymer brushes.<sup>9,10</sup> At the strongly stretched long-chain limit, they found that the density profile approaches a parabolic form, rather than the step function suggested by Alexander and de Gennes. Furthermore, MWC predicted that the distribution of the chain ends spreads through the entire height of the brush.

Despite the success of the MWC theory, deviations from the MWC predictions were found for brush structure in the computer simulations of self-avoiding polymer chains.<sup>14–18</sup> It should be noticed that only ideal chain models are considered in the classical analytic SCF framework and the Gaussian elasticity in the free energy is typically balanced by two-body interactions, which is similar to the Flory theory.<sup>19</sup> However, although the average chain extension is valid in most cases, the Flory theory leads to obvious errors for the individual contributions of elasticity and two-body interactions.<sup>20</sup> Hence, significant deviations should be expected if only one of the two contributions plays a major role, such as the brushes with very low or high grafting densities.<sup>12,21</sup>

Another important problem involving polymer brushes is the interactions between two polymer brushes. This problem is closely related to some applications of polymer brushes, such as the stabilization of colloidal dispersions in ink<sup>22</sup> or minimizing frictional losses between surfaces during shear motion.<sup>23</sup> The interaction between two polymer brushes has also been studied by a variety of experiments,<sup>24–28</sup> theoretical approaches,<sup>10,29–31</sup> and computer simulations.<sup>32–35</sup> The analytic SCF theory is a useful framework for investigating the interaction force of polymer brushes. As a consequence of considering the most probable path of each grafted chain, the MWC theory predicted a free energy profile as a function of the compression distance. This theory makes a good starting point for describing the compression of polymer brushes. Furthermore, the strong-stretch result provides reasonable fitting to some experimental force profiles at appropriate compression distances.<sup>24,27</sup>

For compressed brush systems, molecular dynamic simulation by Murat and Grest<sup>32</sup> also showed clear deviations from the MWC theory for polymer brushes with high grafting

<sup>a)</sup>Authors to whom correspondence should be addressed. Electronic addresses: pingtang@fudan.edu.cn and fengqiu@fudan.edu.cn

densities or at very high compressions. As mentioned above, the two-body interactions considered in the analytic SCF theory lead to obvious deviation if the interaction term plays a major role in the free energy. Unfortunately, the compressed brush systems often encounter this situation. For the polymer brushes with high grafting densities or at very high compressions, the free energy is dominated by the excluded volume interactions. Therefore, the interactions are underestimated if only two-body interactions are included. Another reason may cause the discrepancy is that the MWC's analytic SCF model does not allow the two brushes under compression to interpenetrate due to the assumption of infinitely long chains. Hence, the repulsive force is a result of the change in the configuration entropy, which is exactly the same as the individual brush compressed by a hard wall. In fact, numerical mean-field results,<sup>30</sup> computer simulations,<sup>32–34</sup> and experiments<sup>27,36</sup> for the finite chains showed an obvious interpenetration zone between the two compressed brushes. Recently, based on the interpenetration between the two compressed brushes, Kreer and Balko obtained a new scaling behavior between the repulsive force and the compression distance using a new scaling theory.<sup>31</sup>

In the current work, we develop a classical density functional theory (DFT) to investigate the behavior of compressed polymer brushes. Over the past few decades, classical DFT has provided a fruitful approach to the modeling of microscopic structures and phase behavior of complex fluids.<sup>37,38</sup> Previous publications have also demonstrated that DFT can quantitatively capture the characteristics of tethered chains.<sup>39–47</sup> Particularly, for a hard-sphere chain model, the DFT can treat the fine details of the excluded volume effects between the segments of the grafted chains explicitly, rather than the simple two-body interactions as in the classical analytic SCF theory. This feature makes the DFT a preferred theoretical framework to investigate the compressed brush systems, especially for the brushes with high grafting densities or at high compressions. A comparison between the brush-wall compression and the brush-brush compression can be used to illustrate the effect of the chain interpenetration. Since we concentrate on the influence of the excluded volume effects, the interactions between the segments or between the segment and the solvent are restricted to a simple hard-sphere potential in the current work. Furthermore, the implementation of DFT is carried out for relatively short grafted chains.

The remainder of this paper is organized as follows. Section II introduces the compressed brushes model and the DFT formulation of the tethered hard-sphere chains.

Section III presents the numerical results and corresponding discussion. Section IV summarizes the main results.

## II. THEORETICAL FRAMEWORK

### A. The model

We consider two model systems, brush-wall compression and brush-brush compression, composed of hard-sphere chains grafted on substrates. Schematic diagrams of the models are shown in Figure 1. The polymer chains with one of their end segments grafted to the substrate are modeled as freely jointed hard spheres with a diameter  $\sigma_p$ . The hard-sphere brushes are in vacuum or immersed in a solvent.  $D$  denotes the distance between the two hard walls, and  $N$ ,  $\rho_g$ , and  $\sigma_s$  represent the segment number in each chain, the grafting density (i.e., the grafted chain numbers per unit surface area), and the diameter of solvent sphere, respectively.

For simplicity, we choose  $\sigma_p = \sigma_s = 1$  in this work. Furthermore, it is assumed that all the segments of the polymer chain (except the tethered end-segment) and solvent particles interact with the wall via a hard-wall potential,

$$v_\alpha(z) = \begin{cases} \infty, & z \leq \sigma_\alpha/2 \text{ or } z \geq D - \sigma_\alpha/2 \\ 0, & z > \sigma_\alpha/2 \text{ or } z < D - \sigma_\alpha/2 \end{cases}, \quad (1)$$

where  $z$  denotes the perpendicular distance from the wall and  $\alpha$  represents the polymer or the solvent. It should be noticed that the interaction between the solvent and the segment is assumed to be the same as that between the segments, thus, the solvent particles are treated as non-bonded monomers. The first segment of a polymer chain is tethered to the neutral hard wall, so that the bonding potential  $V_b(\mathbf{R})$  is determined from

$$\exp[-\beta V_b(\mathbf{R})] = k \delta(z_1 - B) \prod_{i=1}^{N-1} \delta(|\mathbf{r}_{i+1} - \mathbf{r}_i| - \sigma_p), \quad (2)$$

where  $\mathbf{R} \equiv (r_1, \dots, r_N)$  is a set of coordinates specifying the positions of the segments in a polymer chain.  $\beta = 1/k_B T$  in which  $k_B$  is the Boltzmann constant and  $T$  is the absolute temperature.  $z_1$  is the perpendicular distance of the center of the tethered segment from the wall.  $\delta$  is the Dirac-delta function, and  $k$  is a normalization constant. The constant  $B = \sigma_p/2$  for the brush grafted on the left substrate, and  $B = D - \sigma_p/2$  for the brush grafted on the right substrate.

Throughout this work, we consider the hard-sphere brushes in vacuum or immersed in a solvent. The hard-sphere brush in vacuum represents a “dry” brush at a sufficiently

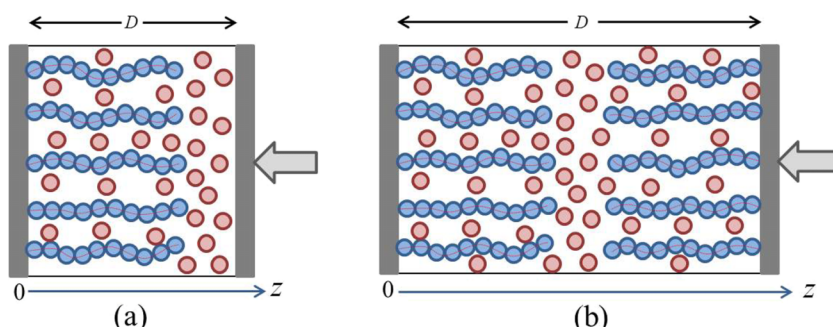


FIG. 1. Two compressed brush systems considered in this work. (a) The grafted hard-sphere chains are compressed by a bare hard wall (brush-wall compression). (b) Two brushes grafted onto the two opposite hard walls interact with each other (brush-brush compression). The blue and red spheres represent the segments of hard-sphere chains and solvents, respectively.

high temperature, in which fluctuations are important and the ideal step-function density profile of the “dry” brush should be perturbed (i.e., fluctuations in the thickness of the grafting layer). The structures of high-temperature “dry” brushes are similar to that of room-temperature brushes in good solvents. In this paper, the brush in vacuum and in solvent can be referred to as the brush “in continuum solvent” and “in explicit solvent”, respectively.<sup>39</sup> On the other hand, since the first segment of each polymer chain is tangentially grafted onto the hard wall, the number of grafted polymer chains is fixed when the grafting density  $\rho_g$  is specified. The form of the bonding potential in Eq. (2) indicates that the polymer segments cannot extend to distances greater than  $z = N\sigma_p$ . Furthermore, in solvent systems, the amount of solvents is kept in equilibrium with a reservoir where the chemical potential of the solvents is given. Thus, a semigrand canonical ensemble is more appropriate for the description of the solvent system.<sup>45</sup>

## B. Density functional theory

In this section, we will introduce the classical DFT for tethered hard-sphere chains. We define several types of densities at first:  $\rho_p(\mathbf{R})$  is the chain number density as a function of chain conformation  $\mathbf{R}$ ,  $\rho_{sol}(\mathbf{r})$  is the number density of the hard-sphere solvents. The local number density of a particular segment  $\rho_{s,i}(\mathbf{r})$  and the local total segment density  $\rho_p(\mathbf{r})$  are introduced via

$$\rho_p(\mathbf{r}) = \sum_{i=1}^N \rho_{s,i}(\mathbf{r}) = \sum_{i=1}^N \int d\mathbf{R} \delta(\mathbf{r} - \mathbf{r}_i) \rho_p(\mathbf{R}). \quad (3)$$

The expression for the Helmholtz free energy functional is chosen according to the theory developed by Yu and Wu.<sup>48</sup> This form of density functional combines the fundamental measure theory (FMT)<sup>49</sup> for the excluded volume effects and the first-order perturbation theory (TPT1)<sup>50</sup> for the chain connectivity. For mixtures of hard-sphere solvents and grafted hard-sphere chains, the Helmholtz free energy functional,  $F[\rho_p(\mathbf{R}), \rho_{sol}(\mathbf{r})]$ , can be divided into an ideal gas part and an excess part due to the intra- and inter-molecular interactions,

$$F[\rho_p(\mathbf{R}), \rho_{sol}(\mathbf{r})] = F_{id}[\rho_p(\mathbf{R}), \rho_{sol}(\mathbf{r})] + F_{ex}[\rho_p(\mathbf{R}), \rho_{sol}(\mathbf{r})]. \quad (4)$$

The ideal gas term can be expressed exactly as

$$\begin{aligned} \beta F_{id}[\rho_p(\mathbf{R}), \rho_{sol}(\mathbf{r})] &= \int d\mathbf{R} \rho_p(\mathbf{R}) [\ln \rho_p(\mathbf{R}) - 1] \\ &\quad + \beta \int d\mathbf{R} \rho_p(\mathbf{R}) V_b(\mathbf{R}) \\ &\quad + \int d\mathbf{r} \rho_{sol}(\mathbf{r}) [\ln \rho_{sol}(\mathbf{r}) - 1]. \end{aligned} \quad (5)$$

The excess term of the Helmholtz free energy is attributed to the hard-sphere repulsion and the intramolecular chain connectivity due to the excluded volume effects. These interactions can be accounted for using the segment densities,

$$\begin{aligned} F_{ex}[\rho_p(\mathbf{r}), \rho_{sol}(\mathbf{r})] &= F_{ex}^{hs}[\rho_p(\mathbf{r}), \rho_{sol}(\mathbf{r})] \\ &\quad + F_{ex}^{chain}[\rho_p(\mathbf{r}), \rho_{sol}(\mathbf{r})]. \end{aligned} \quad (6)$$

According to the modified FMT,<sup>51</sup> the hard-sphere repulsion of the excess Helmholtz free energy can be represented by

$$\begin{aligned} \beta F_{ex}^{hs} &= \int d\mathbf{r} [-n_0 \ln(1 - n_3) + \frac{n_1 n_2 - \mathbf{n}_{V_1} \cdot \mathbf{n}_{V_2}}{1 - n_3} \\ &\quad + \frac{[n_3 + (1 - n_3)^2 \ln(1 - n_3)](n_2^3 - 3n_2 \mathbf{n}_{V_2} \cdot \mathbf{n}_{V_2})}{36\pi n_3^2(1 - n_3)^2}], \end{aligned} \quad (7)$$

where  $n_\alpha(\mathbf{r})(\alpha = 0, 1, 2, 3, V_1, V_2)$  are the scalar and vector weighted densities which are obtained as convolutions of the total particle density and the corresponding weight functions.<sup>48</sup> The contribution of the intramolecular chain connectivity is evaluated from TPT1,<sup>50</sup>

$$\beta F_{ex}^{chain} = \int d\mathbf{r} \frac{1 - N}{N} n_{0P} \xi_P \ln y_{11}^{hs}(\sigma_p, n_\alpha). \quad (8)$$

In the above,  $\xi_P = 1 - \mathbf{n}_{V_{2P}} \cdot \mathbf{n}_{V_{2P}}/n_{2P}^2$  and  $y_{11}^{hs}(\sigma_p, n_\alpha)$  is given by the Boublik-Mansoori-Carnahan-Starling-Leland expression for the contact value of the radial distribution function of segments in a mixture of hard spheres,<sup>52</sup>

$$y_{11}^{hs}(\sigma_p, n_\alpha) = \frac{1}{1 - n_3} + \frac{n_2 \sigma_p \zeta}{4(1 - n_3)^2} + \frac{n_2^2 \sigma_p^2 \zeta}{72(1 - n_3)^3}, \quad (9)$$

with  $\zeta = 1 - \mathbf{n}_{V_2} \cdot \mathbf{n}_{V_2}/n_2^2$ .

The equilibrium density profiles for the polymer segments and solvents are obtained by minimizing the grand potential

$$\frac{\delta \Omega}{\delta \rho_p(\mathbf{R})} = \frac{\delta \Omega}{\delta \rho_{sol}(\mathbf{r})} = 0. \quad (10)$$

The grand potential functional in Eq. (10) is related to the Helmholtz free energy functional by a Legendre transformation,

$$\begin{aligned} \Omega[\rho_p(\mathbf{R}), \rho_{sol}(\mathbf{r})] &= F[\rho_p(\mathbf{R}), \rho_{sol}(\mathbf{r})] \\ &\quad + \int [\psi_p(\mathbf{R}) - \mu_p] \rho_p(\mathbf{R}) d\mathbf{R} \\ &\quad + \int [\psi_{sol}(\mathbf{r}) - \mu_{sol}] \rho_{sol}(\mathbf{r}) d\mathbf{r}, \end{aligned} \quad (11)$$

where  $\mu_p$  and  $\mu_{sol}$  are the chemical potentials of grafted hard-sphere chains and hard-sphere solvents, respectively.  $\psi_p(\mathbf{R})$  and  $\psi_{sol}(\mathbf{r})$  are external potentials exerting on the polymers and solvents, respectively. Here,  $\psi_p(\mathbf{R}) = \sum_{i=1}^N \psi_p(\mathbf{r}_i)$ , where  $\psi_p(\mathbf{r}_i)$  is the external potential on individual segments. Minimization of the grand potential yields a set of Euler-Lagrange equations,

$$\rho_p(\mathbf{R}) = \exp[\beta \mu_p - \beta \psi_p(\mathbf{R}) - \beta V_b(\mathbf{R}) - \frac{\delta \beta F_{ex}}{\delta \rho_p(\mathbf{R})}], \quad (12)$$

$$\rho_{sol}(\mathbf{r}) = \exp[\beta \mu_{sol} - \beta \psi_{sol}(\mathbf{r}) - \frac{\delta \beta F_{ex}}{\delta \rho_{sol}(\mathbf{r})}]. \quad (13)$$

For systems with the density profiles changing only in the  $z$ -direction, by combining with Eq. (3), Eqs. (12) and (13) can be simplified to

$$\rho_p(z) = k \exp(\beta \mu_p) \sum_{i=1}^N \{\exp[-\beta \lambda_p(z)] G_g^i(z) G_f^i(z)\}, \quad (14)$$

$$\rho_{sol}(z) = \exp[\beta \mu_{sol} - \beta \psi_{sol}(z) - \frac{\delta \beta F_{ex}}{\delta \rho_{sol}(z)}], \quad (15)$$

with  $\lambda_p(z) = \delta F_{\text{ex}}/\delta\rho_p(z) + \psi_p(z_i)$ . The propagator functions  $G_g^i(z)$  and  $G_f^i(z)$  represent the connectivity of the polymer chains, starting from the grafted end and the free end, respectively. These functions are determined from the recurrence relation,

$$G_g^i(z) = 2\pi\sigma_p \int dz' \exp[-\beta\lambda_p(z')] \theta(\sigma_p - |z - z'|) G_g^{i-1}(z'), \quad (16)$$

for  $i = 3, \dots, N$  with

$$G_g^2(z) = 2\pi\sigma_p \exp[-\beta\lambda_p(B)] \theta(\sigma_p - |z - B|) \quad (17)$$

and

$$G_f^i(z) = 2\pi\sigma_p \int dz' \exp[-\beta\lambda_p(z')] \theta(\sigma_p - |z - z'|) G_f^{i+1}(z'), \quad (18)$$

for  $i = 1, \dots, N-1$  with  $G_f^N(z) = 1$ .

Particularly, the density distribution of the tethered segments is given by

$$\rho_{s,i}(z) = \rho_g \delta(z - B). \quad (19)$$

The coefficient  $k \exp(\beta\mu_p)$  in Eq. (14) can be considered as a constant, which is determined by the normalization condition applied to each segment,

$$\int \rho_{s,i}(z) dz = \rho_g \quad (i = 2, 3, \dots, N). \quad (20)$$

We solve Eqs. (16) and (18) by using conventional Picard iteration method.<sup>53</sup> The final results are obtained when the difference between the input and output for density is smaller than 0.001. The numerical integrations are calculated with a step size of  $\Delta z = 0.001\sigma_p$ .

### C. Solvation force

In this work, the solvation force  $f$  between the two hard walls is used to characterize the interaction between the polymer brush and wall, or the two polymer brushes. Physically, the solvation force is the force that must be exerted on the walls in order to maintain a constant separation  $D$ . The force per unit area can be calculated from<sup>54</sup>

$$f/k_B T = -\frac{1}{A} \frac{\partial \Omega}{\partial D} - P, \quad (21)$$

where  $A$  is the area of the grafting surface and  $P$  is the pressure of the bulk system. Combining with Eqs. (11) and (21) can be simplified to

$$f/k_B T = - \int_0^D \frac{\partial \psi(z)}{\partial z} \rho(z) dz - P, \quad (22)$$

where  $\psi(z)$  and  $\rho(z)$  represent the interaction potential between the molecules and the wall and the total density of molecules, respectively. In the case of two hard walls,

$$f/k_B T = \rho(0) + \rho(D) - P. \quad (23)$$

The bulk pressure  $P$  can be calculated at the limit of  $D \rightarrow \infty$ . At this limit, the first term on the right-hand of Eq. (22) becomes equal to the bulk pressure  $P$ .

## III. RESULTS AND DISCUSSION

### A. Density profiles of uncompressed brushes

Before discussing the properties of compressed brushes, it is helpful to investigate the structures of uncompressed brushes composed of hard-sphere chains. Figure 2 shows the number density of grafted hard-sphere chains with 20 monomers ( $N = 20$ ) at different grafting densities. The insets represent the volume density of the monomers  $\phi_p(z)$  which are calculated from the number density  $\rho_p(z)$  using  $\phi_p(r) = 1/V_R \int_{|r'| < \frac{\sigma_p}{2}} d\mathbf{r}' \rho_p(\mathbf{r}' + \mathbf{r})$ , where  $V_R$  is the volume of a monomer sphere. Here, the brush is assumed to be in vacuum and the distance  $D$  between the two hard walls is large enough to ensure that the configurations of the grafted chains are not influenced by the opposite bare wall or brush.

Figure 2 shows that the stretching of the grafted hard-sphere chains increases when the grafting density  $\rho_g \sigma_p^2$  is increased from 0.01 to 0.20. Here, the grafted hard-sphere chains at low grafting densities ( $\rho_g \sigma_p^2 < 0.05$  for  $N = 20$ ) are more likely to be in the “mushroom” state. Compared with the parabolic density profile predicted by the MWC theory,<sup>9,10</sup> our results exhibit qualitatively similar behavior. However,

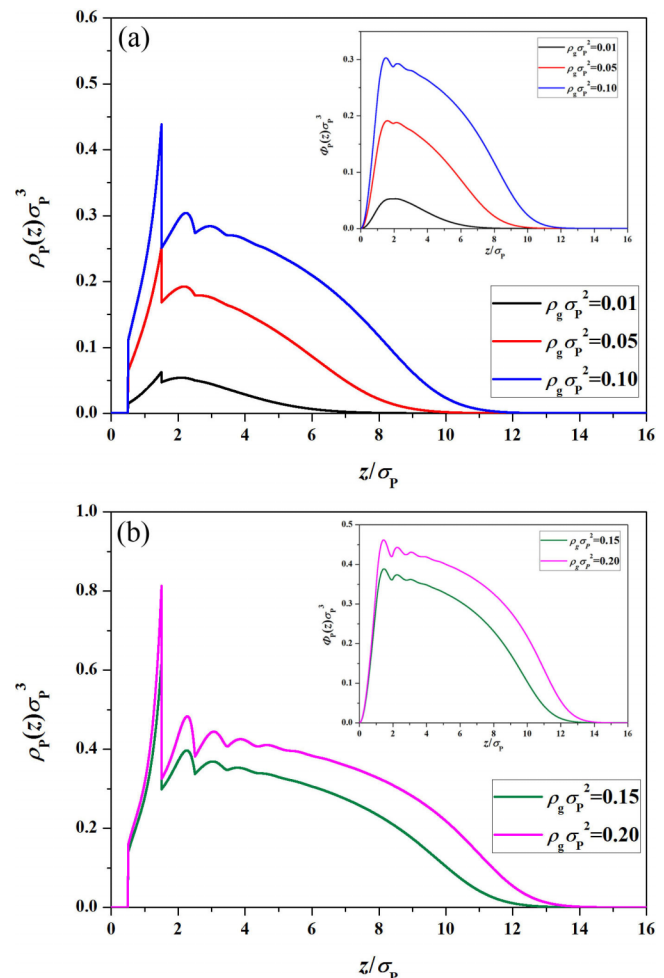


FIG. 2. Monomer number density  $\rho_p(z)\sigma_p^3$  as a function of the distance  $z$  from the grafting surface for  $N = 20$  with different grafting densities. (a) The low grafting densities:  $\rho_g \sigma_p^2 = 0.01, 0.05, 0.10$ , and (b) the relatively high grafting densities:  $\rho_g \sigma_p^2 = 0.15, 0.20$ . Insets: the corresponding monomer volume density  $\phi_p(z)\sigma_p^3$ .

notable deviations from the parabolic profile near the grafting surface and in the outer edge of the brush are observed. It is obvious that the monomers of grafted hard-sphere chains show short-range positional order near the hard wall, especially for the higher grafting densities shown in Figure 2(b). A notable feature is that the monomer number densities at all grafting densities exhibit a drastic jump at  $z/\sigma = 1.5$ . This is because the second segments, which are tangentially connected with the grafted first segments, tend to concentrate at  $z/\sigma = 1.5$  and cannot extend beyond  $z/\sigma = 1.5$ . The density oscillations are originated from the short-range excluded volume interactions that are properly counted in DFT. The density profiles of the brushes with higher grafting densities become smooth at the distance further from the hard wall and tend to be flatter, as shown in Figure 2(b). Furthermore, all the density profiles in Figure 2 exist at a gradually decreasing region at the outer edge of the brushes, rather than a well-defined cutoff in the parabolic profile predicted by the MWC theory.<sup>9,10</sup>

The distribution of the free ends is important for understanding the behavior of a polymer brush. The DFT results of the free end distribution are shown in Figure 3. Similar to the result of the MWC theory,<sup>9,10</sup> the free ends are distributed through the entire height of the brush except for  $z < \sigma_p/2$ , which is the excluded zone due to the hard-wall potential. We also notice that the behavior of the free ends depends on the grafting density. For the low grafting densities ( $\rho_g \sigma_p^2 = 0.01, 0.05$ ) shown in Figure 3(a), the number density of the free ends  $\rho_{\text{end}}(z) \sigma_p^3$  increases convexly before reaching a maximum, then  $\rho_{\text{end}}(z) \sigma_p^3$  decreases to zero gradually. This can be attributed to a large free space between the grafted hard-sphere chains at the low grafting density which allows the free ends to fold back easily. For the higher grafting densities ( $\rho_g \sigma_p^2 = 0.15, 0.20$ ) shown in Figure 3(b), fold back of the free ends is hindered due to the crowded space between the chains. Hence,  $\rho_{\text{end}}(z) \sigma_p^3$  increases gradually to reach its maximum and then decreases to zero rapidly in contrast to the case of relatively low grafting densities. In other words, the free ends tend to locate in the outer region when the grafting density is high enough. These behaviors are qualitatively consistent with the results from molecular dynamics simulations of hard-sphere brushes by Murat and Grest.<sup>14</sup>

Next, we discuss the influence of hard-sphere solvents on the morphology of uncompressed brushes. In contrast to brushes in vacuum, solvent particles, represented by non-bonded hard spheres with an adjustable packing density, are added to the system. Figure 4(a) shows the density profiles of the brushes immersed in the hard-sphere solvents with different bulk densities  $\rho_{\text{sol},b}$ . The distribution of the hard-sphere solvents  $\rho_s(z)$  is presented in the inset. We observe that the solvents are more preferential to aggregate near the wall due to the effects of entropy of hard-sphere solvents. Furthermore, when the total density of the hard-sphere system is high enough (e.g.,  $\rho_{\text{sol},b} = 0.60$ ), the polymer segments also tend to aggregate near the wall. This behavior is similar to the transition from depletion to adsorption as the packing fraction of fluids in a slit increases.<sup>48</sup> For example, when the bulk density of solvents is  $\rho_{\text{sol},b} = 0.60$  (the blue line shown in Figure 4(a)), the average packing fraction in this semigrand canonical ensemble reaches a high value at  $\eta \approx 0.37$  ( $\eta = \pi \rho_b \sigma_p^3 / 6$ ). In this case, the distri-

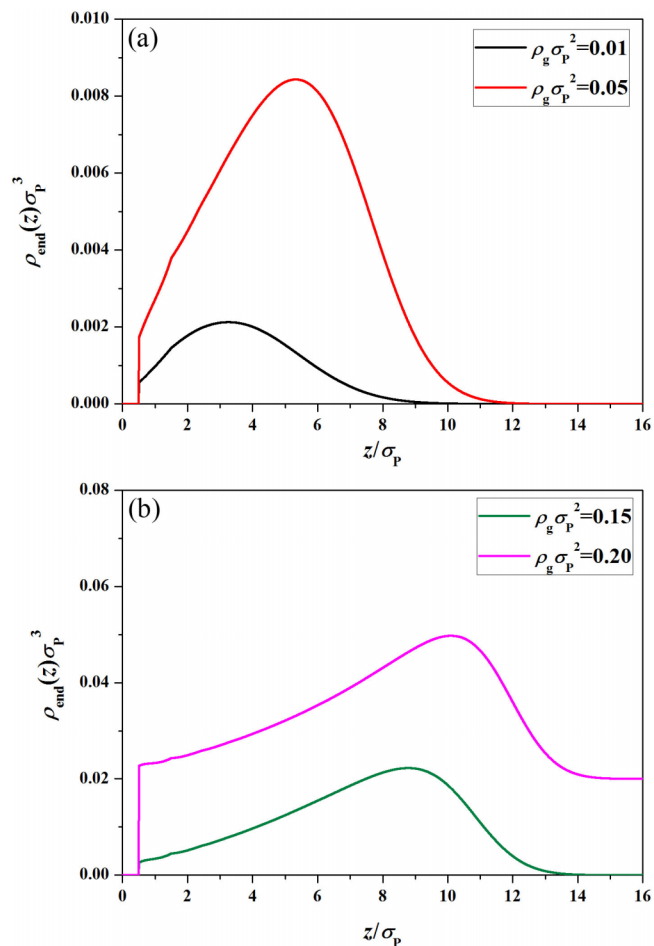


FIG. 3. The distribution of the free ends  $\rho_{\text{end}}(z) \sigma_p^3$  for  $N = 20$  with different grafting densities. The low grafting densities in (a) are  $\rho_g \sigma_p^2 = 0.01, 0.05$ , and the relatively high grafting densities in (b) are  $\rho_g \sigma_p^2 = 0.15, 0.20$ . Here, the number density profile of  $\rho_g \sigma_p^2 = 0.20$  (purple line) is shifted vertically by 0.02 for clear expression.

bution of segments depends primarily on hard-sphere packing, similar to the particle distribution in a monomeric fluid. Thus, the polymer segments aggregate to form an adsorption layer near the wall. However, an inverse phenomenon occurs in the outer part of the brush. The screening effect of hard-sphere solvents with a high packing density prevents the grafted chains extent to the outer space (see the schematic illustration shown in Figure 4(b)). Thus, we observe a decrease in the height of the brush  $h_0$  when the bulk density of solvents  $\rho_{\text{sol},b}$  is increased, as shown in Figure 4(b).

## B. Interpenetration in the compressed brush-brush systems

As mentioned above, the MWC theory does not allow two brushes under compression to interpenetrate due to the assumption of infinitely long chains, so the brush-brush compression and the brush-wall compression are considered to be equivalent.<sup>10</sup> Obviously, this assumption is not valid for the short grafted chains, thus, it is interesting to discuss the differences that arise from the release of this assumption.

The segment number density profile of the brushes compressed by a hard wall is shown in Figure 5(a). Here, the chain

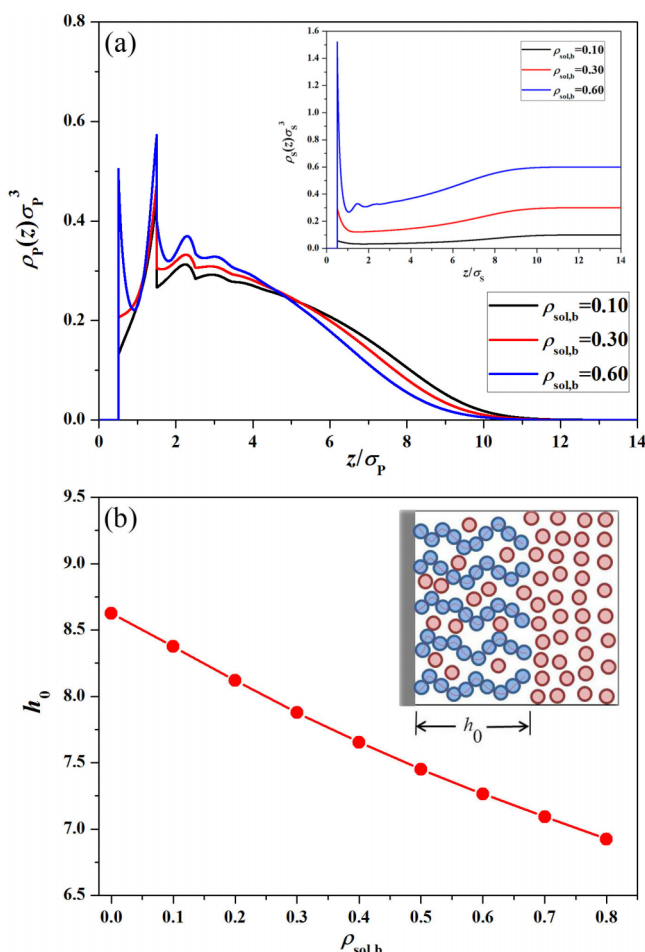


FIG. 4. (a) Monomer number density profile  $\rho_p(z)$  as a function of the distance  $z$  from the grafting surface for  $N = 20$ ,  $\rho_g = 0.10$  in solvents. The bulk density of solvents  $\rho_{\text{sol},b}$  changes from 0.10 to 0.60. Inset: the corresponding number density of hard-sphere solvents  $\rho_s(z)$ . (b) The height of the brush  $h_0$  versus the bulk density of solvents  $\rho_{\text{sol},b}$ . The chain length and the grafting density are the same as those in (a). The height of a brush is calculated by  $h_0 = 2 \int_0^D z \rho_p(z) dz / \int_0^D \rho_p(z) dz$ .<sup>40</sup>

length and the grafting density are fixed at  $N = 20$  and  $\rho_g \sigma_p^2 = 0.10$ . The degree of compression is represented by a reduced compression distance between the surfaces  $d = D/h_0$ , where  $h_0$  is the height of the uncompressed brush. In particular, a small reduced compression distance corresponds to a higher degree of compression. Due to the hard wall potential between the segments and the wall, a depletion layer appears near the hard wall at large reduced distances. When the reduced compression distance is decreased to  $d = 0.30$ , the packing fraction of the polymer segments increases to  $\eta \approx 0.33$ . Here, the packing fraction of grafted polymer chains is calculated by  $\eta = (\rho_p \sigma_p^2 N/D) \pi \sigma_p^3 / 6$ . In this case, two adsorption layers appear near the two walls, which is similar to the behavior of the uncompressed brush in dense solvents mentioned above. The asymmetry of the two adsorption layers can be understood in terms of the conformational entropy change due to the chain grafting on a surface. In the brush-wall compression, the first hard-sphere segments of each chain are fixed on the grafting surface (left surface). These grafted segments are fixed, so their ability to allow other non-grafting segments to fit in the space not occupied by them (which is close to the grafting surface)

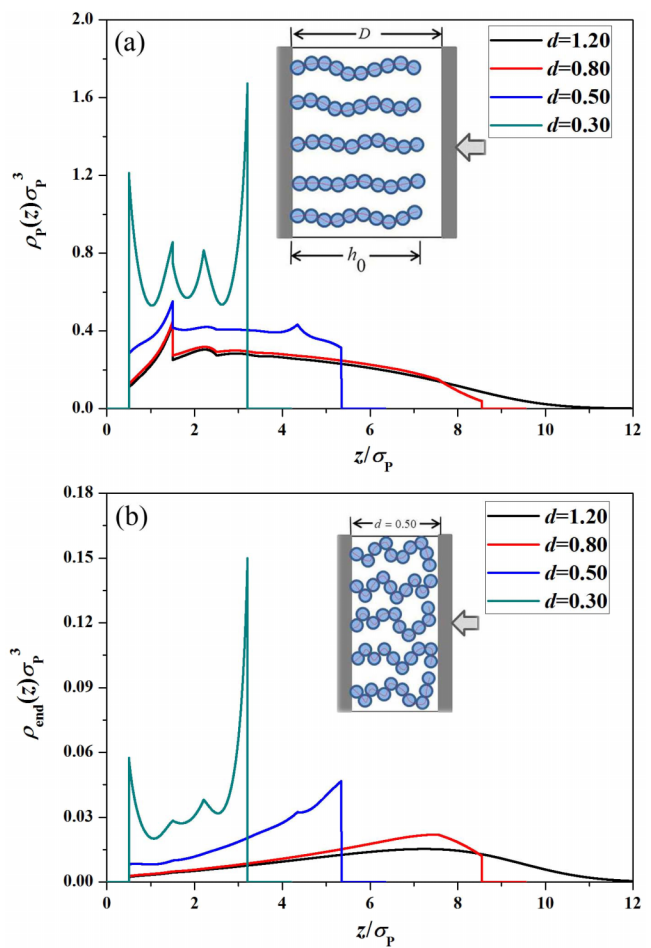


FIG. 5. (a) The number density profile of the brush-wall compression at different reduced compression distances. (b) The distribution of free ends under compression. Here, the grafted chain length and the grafting density are  $N = 20$  and  $\rho_g \sigma_p^2 = 0.10$ , respectively. The brush is in vacuum and the height of an uncompressed brush which is used to normalize the reduced distance is  $h_0 = 10.69$ . A schematic illustration for the compressed brush at  $d = 0.50$  is inserted in (b).

is relatively low. However, on the compressing surface (the surface at right), the (non-grafting) segments are free to move. Under strong compression, the non-grafting segments tend to be adsorbed on both of the surfaces. Obviously, the adsorption on the compressing surface is able to realize more conformations because the movable adsorbed segments can take more positions. Thus, we observe a higher adsorption value nearby the compressing surface under strong compression. Furthermore, we note that the adsorption layer occurs earlier nearby the compressing surface as the reduced compression distance decreases.

Figure 5(b) shows the distribution of free ends under compression. During the compression, the free ends contact with the hard wall at first. A transition from depletion to adsorption for the free ends also occurs near the compressing wall. Based on the distribution of all the segments (data not shown here), we find that the segments near the free ends tend to aggregate near the bare wall at first during compression (see the schematic illustration in Figure 5(b)). Hence, the maximum of the free ends density profile moves towards the compressing hard wall as the reduced compression distance decreases, as shown in Figure 5(b).

Figure 6(a) shows the monomer number density of the brush-brush compression system with  $N = 20$  and  $\rho_g \sigma_p^2 = 0.10$ . In this case, the reduced compression distance is normalized by  $d = D/2h_0$ . One can see that the density increases everywhere between the two hard walls as a decrease of the reduced compression distance and tends to be uniform at the high compression degree. For the reduced distance  $d = 0.30$ , the segments form two well-defined symmetrical layers at the distances  $z = \sigma_p/2$  and  $z = D - \sigma_p/2$ , similar to the formation of the adsorption layer in the brush-wall compression system. The contribution to the total monomer density from the brush on the left substrate is shown in Figure 6(b). Although the compression makes the density increase, the density profile of each brush remains parabolic in a large part until the segments of the left brush contact with the hard wall on the right substrate (e.g.,  $d = 0.30$ ). Furthermore, by comparing Figure 6(b) with Figure 6(a), we find that the brush on the left substrate spreads out beyond the distance  $z > D/2$ , which indicates that an obvious interpenetration exists in the brush-brush compression system. These results are supported by that obtained from numerical SCF calculation<sup>30,55</sup> and computer simulations.<sup>32–34,56</sup>

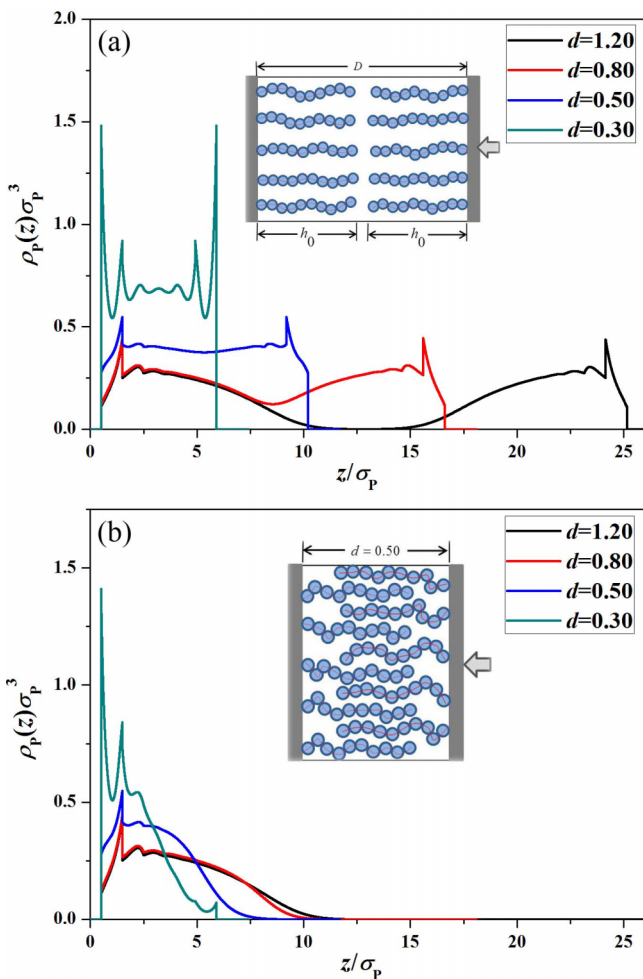


FIG. 6. (a) The total number density profile of two brushes system at different reduced compression distances. (b) The contribution to the total monomer number density from the brush on the left substrate. The chain length and the grafting density are the same as those in Figure 5, but the reduced compression distance  $d$  is normalized by  $2h_0$ . A schematic illustration for the compressed brushes at  $d = 0.50$  is inserted in (b).

To quantify the extent of the interpenetration between the two compressed brushes at a separation  $D$ , we define the overlap integral,  $I(D)$ , by

$$I(D) = \frac{D}{\theta_1 \theta_2} \int_0^D \rho_{P,L}(z) \rho_{P,R}(z) dz, \quad (24)$$

where  $\rho_{P,L}(z)$  and  $\rho_{P,R}(z)$  are the density profile for the brush on the left and right sides, respectively, and  $\theta_1$  and  $\theta_2$  are calculated by  $\theta_1 = \int_0^D \rho_{P,L}(z) dz$  and  $\theta_2 = \int_0^D \rho_{P,R}(z) dz$ , which are the total grafted amount of each brush between the two hard walls. Here,  $I(D)$  is defined to be unity in the limit of total interpenetration where the two brushes are uniformly distributed throughout the volume, i.e.,  $I(D) = 1.0$ .<sup>57</sup> Figure 7 shows the interpenetration extent profile  $I(D)$  for  $N = 20$  with different grafting densities. We notice that Murat and Grest proposed a simple scaling law that correlates the interpenetration and the reduced compression distance based on the results of molecular dynamics simulations.<sup>32</sup> However, this scaling result is only appropriate for the brushes under slight compressions or with low grafting densities. Figure 7 indicates the grafting density has a significant influence on the interpenetration of the two compressed brushes. At the same reduced compression distance, the lower the grafting density  $\rho_g \sigma_p^2$ , the larger the interpenetration extent  $I(D)$ . This can be explained by that the higher grafting density results in more crowded spaces between the segments, so they are more difficult to interpenetrate when the two brushes interact with each other. On the other hand, two compressed brushes with higher grafting density can lead to more uniform density profile at a smaller compression distance. In the uniform density region, further compression may cause a uniform compression rather than an increase in the interpenetration.<sup>32</sup>

### C. Repulsive force of compressed brushes

In this part, we discuss the DFT results for the interaction forces of brush-wall compression and brush-brush compression systems. The MWC theory<sup>10,29</sup> predicts that the free

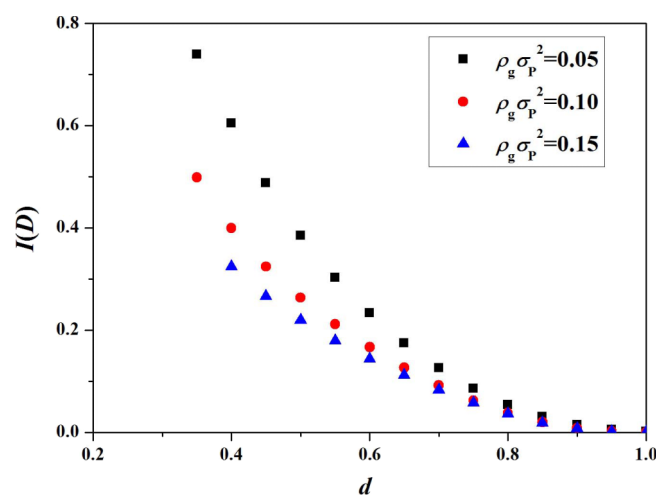


FIG. 7. The extent of the interpenetration  $I(D)$  between two compressed brushes as a function of the reduced compression distance  $d = D/2h_0$  for  $N = 20$  with different grafting densities. The brushes are in vacuum and the uncompressed brush height  $h_0$  is 8.72, 10.69, 12.04, for  $\rho_g \sigma_p^2 = 0.05, 0.10, 0.15$ , respectively.

energy per chain under compression is given by

$$F(d) = N(\rho_g w)^{2/3} (\pi^2/12)^{1/3} \left[ \frac{1}{2d} + \frac{1}{2} d^2 - \frac{1}{10} d^5 \right], \quad (25)$$

where  $w$  represents the excluded volume parameter,  $d$  is the reduced compression distance. The force per unit area can be calculated by  $\partial F(d)/\partial d$ , leading to the force  $f(d) \sim (-1/2 d^{-2} + d - 1/2 d^4)$ . This result of the interacting force is based on the brush compressed by a hard wall due to the assumption of infinitely long chains.

Figure 8 shows the solvation force per unit area of the brush-wall compression system for  $N = 20$ . In Figure 8(a), one can see that the force between the hard-sphere brush and the hard wall is always repulsive. At the same reduced distance, the repulsive force is larger for the brush with a higher grafting density. This is easily understood by noting that the compression for denser matters needs larger pressure. In Figure 8(b), we compare our DFT results with the MWC result in the double-logarithmic scale. The prefactor in Eq. (25) is

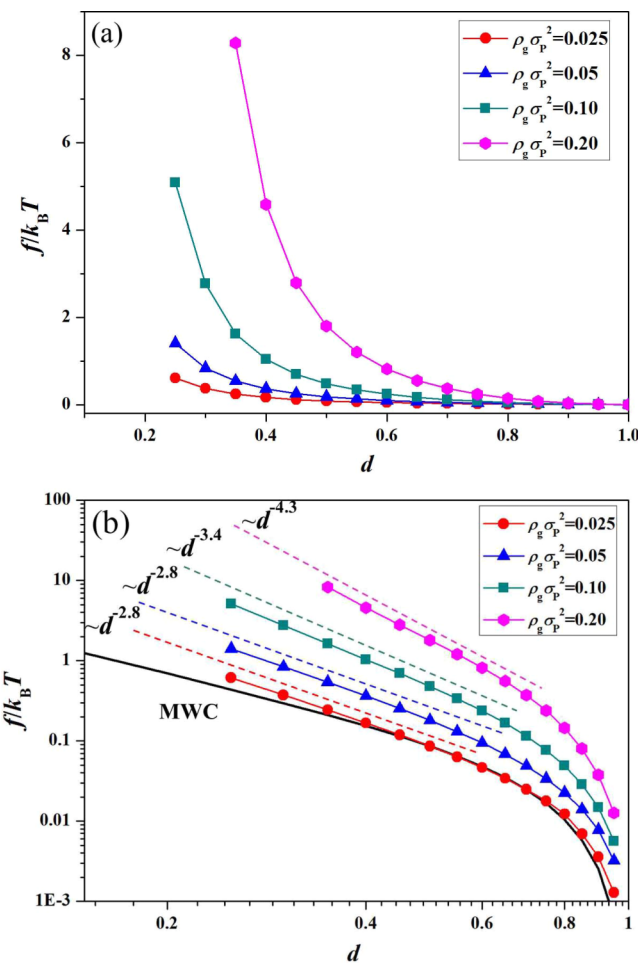


FIG. 8. The repulsive force per unit area of the brush-wall compression for  $N = 20$  with different grafting densities. (a) The force profile  $f$  versus the reduced compression distance  $d = D/h_0$ . The uncompressed brush height  $h_0$  is 7.19, 8.72, 10.69, 13.12, for  $\rho_g \sigma_p^2 = 0.025, 0.05, 0.10, 0.20$ , respectively. (b) The DFT results are in comparison with the MWC force profile in the double-logarithmic scale. Here, the black solid line is the result of MWC theory. The prefactor in Eq. (25) is chosen to give best fit to the force profile of  $\rho_g \sigma_p^2 = 0.025$ . The dotted lines mean the fitting results in the relatively high compression regions and the slopes of these fitting lines are marked out in different colors.

chosen to give the best fit to the force profile of  $\rho_g \sigma_p^2 = 0.025$ . We observe that the compression force of  $\rho_g \sigma_p^2 = 0.025$  is consistent with the MWC profile, with deviation occurring at the reduced compression distance  $d = 0.40$ . This deviation can be attributed to the underestimation of excluded volume interactions in the MWC theory for dense systems. For this reason, we concentrate on the result of DFT at the relatively high compression regime. In the limit of high compression, the reduced distance  $d$  is small, thus, the term  $d^{-2}$  is the dominate contribution to the repulsive force. The force profiles of  $\rho_g \sigma_p^2 = 0.05 - 0.20$  in Figure 8(b) also exist linear regions for the relatively high compression in the double-logarithmic scale. We find that the index  $x$  in  $f(d) \sim d^{-x}$  increases from 2.8 to 4.3 when the grafting density  $\rho_g \sigma_p^2$  is increased from 0.05 to 0.20, but the index of  $\rho_g \sigma_p^2 = 0.025$  approximately equals to that of  $\rho_g \sigma_p^2 = 0.05$ . Although the force behavior in brush-wall compressions has rarely been reported, similar grafting density dependence of force profile can be found in molecular dynamic simulations of the brush-brush compression system.<sup>32</sup> The higher grafting density means larger compression force and faster increase in the force when the reduced compression distance is decreased. For the low grafting densities ( $\rho_g \sigma_p^2 = 0.025, 0.05$ ), the packing of the segments is dilute even at the high compression, thus, the dependence on the grafting density for the index  $x$  in  $f(d) \sim d^{-x}$  disappears. However, the index  $x$  obtained by our DFT theory is higher than that of the MWC theory even at a low grafting density. This difference is originated from the different treatments of the excluded volume interactions.

Figure 9 shows the repulsive force between two compressed brushes in the double-logarithmic scale. The force profiles in the relatively high compression regions are fitted linearly, similar to that shown in Figure 8(b). We also find the dependence on the grafting density for the index  $x$  in  $f(d) \sim d^{-x}$ . The index  $x$  approximately equals to 3.4, 3.6, 4.1 and 5.3, respectively, when the grafting density  $\rho_g \sigma_p^2$  is increased from 0.025 to 0.20. In a recent publication,<sup>31</sup> Kreer and Balko found a scaling behavior  $f(d) \sim d^{-3.5}$  in the high compression

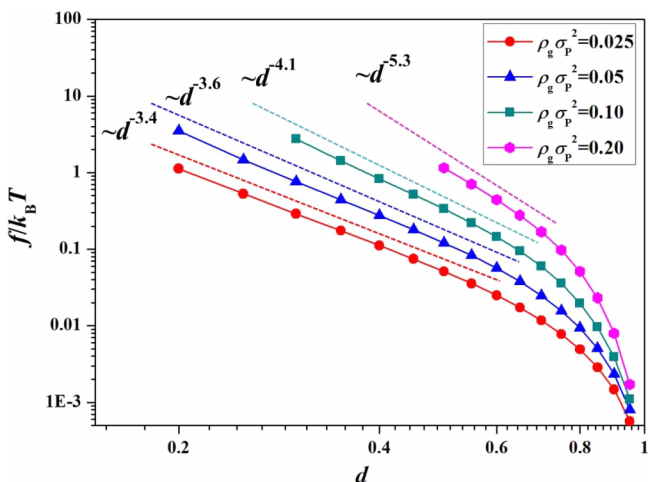


FIG. 9. The repulsive force per unit area between two compressed brushes as a function of the reduced compression distance  $d = D/2h_0$  for  $N = 20$  with different grafting densities. The dotted lines mean the linearly fitting results for the force profile in the relatively high compression regions and the slopes of these fitting lines are marked out in different colors.

region between two brushes using a novel scaling theory. This relationship between the force and the reduced compression distance is roughly suitable for the results in Figure 9 at the low grafting densities, i.e.,  $\rho_g \sigma_p^2 = 0.025, 0.05$ . However, it is still invalid for the brushes with higher grafting densities. It should be noticed that this theory is based on an assumption which considers the repulsive force is completely determined by the interpenetration between the two brushes under intermediate compressions. Based on the results in Figure 7, we find that the interpenetration between two compressed brushes is suppressed at the high grafting densities. Thus, the assumption in Kreer and Balko's theory may underestimate the repulsive force for the compressed brushes with relatively high grafting densities.

A direct comparison between the brush-wall and the brush-brush compression is made in Figure 10 for  $N = 20$  and  $\rho_g \sigma_p^2 = 0.05, 0.10$ . We observe that the repulsive force of the brush-brush compression is smaller than that of the brush-wall compression, but the former increases more rapidly as the reduced distance is decreased. In the limit of high compression, the repulsive forces of these tend to be the same. The most significant difference between these two systems is that there is an interpenetration zone in the case of brush-brush compression, indicating that the brush-brush interaction is much "softer" than the brush-wall interaction. Thus, we observe a smaller repulsive force in the brush-brush compression system. Furthermore, in the limit of high compression, the polymer segments between the two hard walls become crowded. A further decrease in the reduced compression distance causes a uniform compression rather than an increase in the interpenetration. In this regime, the compression behavior of brush-brush is similar to the brush-wall system.

Finally, we also investigate the behavior of the compressed brushes immersed in a hard-sphere solvent. Figure 11(a) shows the force profiles of the brush-wall compression systems which are immersed in solvents with bulk densities  $\rho_{\text{sol},b} = 0, 0.20, 0.40$ , respectively. The  $\rho_{\text{sol},b} = 0$  means the brush is in vacuum. We find that the addition of hard-sphere solvents has no signif-

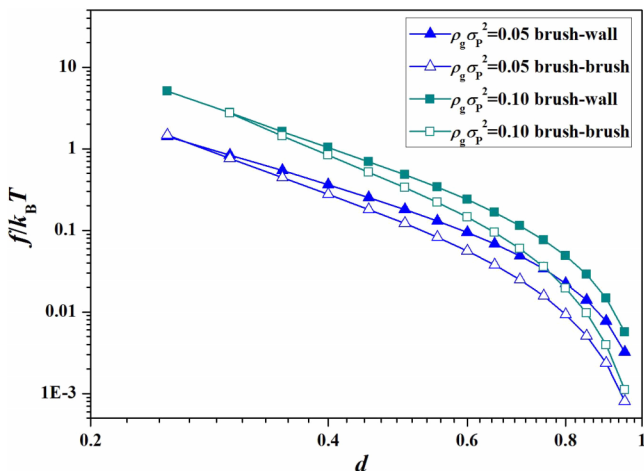


FIG. 10. The comparison for the repulsive force between the brush-wall compression (solid symbol) and the brush-brush compression (open symbol) for  $N = 20$  and  $\rho_g \sigma_p^2 = 0.05, 0.10$ . The reduced compression distance  $d$  represents  $D/h_0$  for the brush-wall system and  $D/2h_0$  for the brush-brush system.

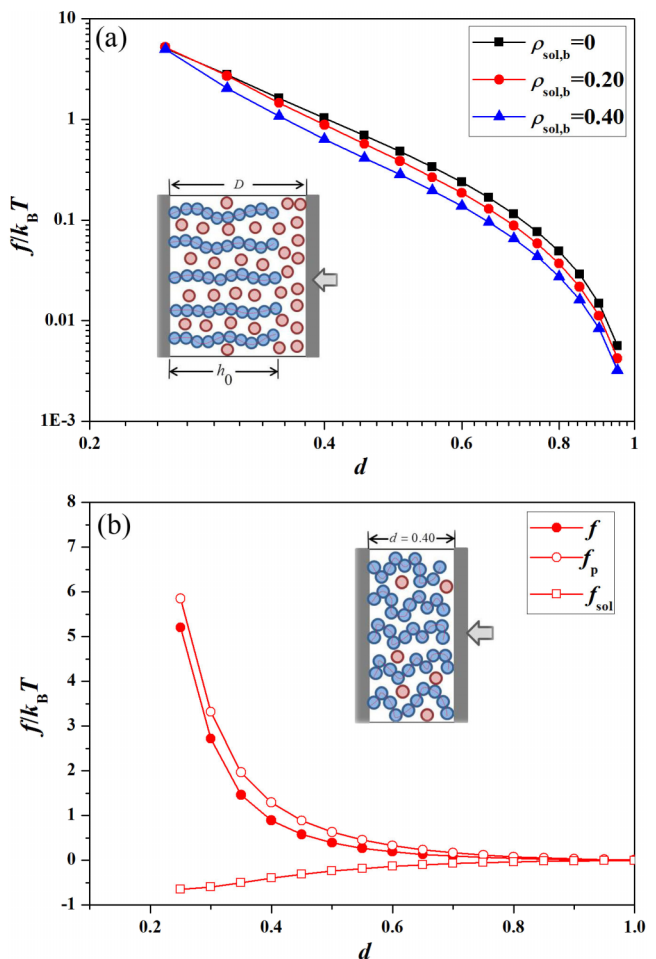


FIG. 11. The solvation force per unit area in the brush-wall compression system immersed in the hard-sphere solvents for  $N = 20$  and  $\rho_g \sigma_p^2 = 0.10$ . (a) The compression force profiles with the different bulk densities of solvents  $\rho_{\text{sol},b}$  in the double-logarithmic scale. (b) The contribution to the solvation force from the polymer (open circle) and the solvent (open square) for  $\rho_{\text{sol},b} = 0.20$ . A schematic illustration for the squeezing out of the solvents at the reduced compression distance  $d = 0.40$  is sketched out in (b).

ificant influence on the trend of the force profile over a wide compression region. The main effect of solvents is reflected by the decrease in the repulsive force when the solvents are added. However, the effects of hard-sphere solvents tend to decrease during the compression, leading to almost the same repulsive forces in the limit of high compression, as shown in Figure 11(a). To discuss the influence of solvents in detail, we divide the solvation force into two parts: the contribution from the polymers  $f_p$  and the solvents  $f_{\text{sol}}$ , respectively. In Figure 11(b), one can see that  $f_{\text{sol}}$  calculated from Eq. (23) is always negative, thus, the total force due to solvents is smaller than that in vacuum. The negative  $f_{\text{sol}}$  means that the density of hard-sphere solvents is always decreasing during the compression in this semigrand canonical system. In the limit of high compression, the solvents are almost all squeezed out of the narrow slit (see the schematic illustration in Figure 11(b)), then the  $f_p$  dominates the total repulsive force and its behavior tends to be the same as the compressed brush in vacuum. The influence of the hard-sphere solvents on the brush-brush compression system is similar to the brush-wall system (data not shown here).

#### IV. CONCLUSIONS

In summary, we have investigated the behavior of compressed polymer brushes with relatively short hard-sphere chains using the classical DFT. The main objective of the current study is to provide a more accurate description of the excluded volume effects for the compressed brush system, rather than the simple two-body interactions in the classical analytic SCF theory. As a benchmark test of the DFT theory, we applied the theory to examine the structures of uncompressed hard-sphere brushes in vacuum or immersed in a hard-sphere solvent. Our DFT results on the main features of polymer brushes, including the parabolic density profile, the distribution of free ends, the adsorption layer in a dense solvent, are in qualitative agreement with the analytic theory and simulations.

For the compression behavior of the hard-sphere brushes, we consider two compression types: brush-wall compression and brush-brush compression. We find that an obvious interpenetration zone exists in the case of brush-brush compression and the extent of the interpenetration depends strongly on the grafting density. More importantly, we calculate the repulsive force as a function of reduced compression distance. The force profile for the case of brush-wall compression is presented and compared with the MWC theory.<sup>10,29</sup> The force of DFT results increases more rapidly during compression for the brushes with high grafting densities or at the high compressions, where the excluded volume interactions play a major role in determining the free energy. In the case of brush-brush compression, the repulsive force is smaller than that of the brush-wall system at the same reduced compression distance. It means that the interpenetration between compressed brushes creates a “softer” interaction. We also compare our DFT results for the case of brush-brush compression with the recent scaling theory by Kreer and Balko.<sup>31</sup> The result shows that the force behavior predicted by their theory only provides a qualitative description of the hard-sphere brushes with low grafting densities. The influence of hard-sphere solvents on the behavior of compressed brush is also discussed.

#### ACKNOWLEDGMENTS

We gratefully acknowledge the financial support from the National Natural Science Foundation of China (Grant Nos. 21320102005 and 21374023) and National Basic Research Program of China (Grant No. 2011CB605700). A.C.S. acknowledges the support from the Natural Sciences and Engineering Research Council (NSERC) of Canada.

<sup>1</sup>S. T. Milner, *Science* **251**, 905 (1991).

<sup>2</sup>W. J. Yang, K. G. Neoh, E. T. Kang, S. L. M. Teo, and D. Rittschof, *Prog. Polym. Sci.* **39**, 1017 (2014).

<sup>3</sup>W. Senaratne, L. Andruzzini, and C. K. Ober, *Biomacromolecules* **6**, 2427 (2005).

<sup>4</sup>B. Zhao and W. J. Brittain, *Prog. Polym. Sci.* **25**, 677 (2000).

- <sup>5</sup>K. Binder and A. Milchev, *J. Polym. Sci., Part B: Polym. Phys.* **50**, 1515 (2012).
- <sup>6</sup>S. Alexander, *J. Phys. (Paris)* **38**, 983 (1977).
- <sup>7</sup>P. G. de Gennes, *J. Phys. (Paris)* **37**, 1445 (1976).
- <sup>8</sup>P. G. de Gennes, *Macromolecules* **13**, 1069 (1980).
- <sup>9</sup>S. T. Milner, T. A. Witten, and M. E. Cates, *Europhys. Lett.* **5**, 413 (1988).
- <sup>10</sup>S. T. Milner, T. A. Witten, and M. E. Cates, *Macromolecules* **21**, 2610 (1988).
- <sup>11</sup>D. F. K. Shim and M. E. J. Cates, *J. Phys. (Paris)* **50**, 3535 (1989).
- <sup>12</sup>P. Y. Lai and A. Halperin, *Macromolecules* **24**, 4981 (1991).
- <sup>13</sup>P. M. Biesheuvel, W. M. de Vos, and V. M. Amoskov, *Macromolecules* **41**, 6254 (2008).
- <sup>14</sup>G. S. Grest and M. Murat, *Macromolecules* **22**, 4054 (1989).
- <sup>15</sup>A. Chakrabarti and R. Toral, *Macromolecules* **23**, 2016 (1990).
- <sup>16</sup>R. Dickman and D. C. Hong, *J. Chem. Phys.* **95**, 4650 (1991).
- <sup>17</sup>P. Y. Lai and K. Binder, *J. Chem. Phys.* **95**, 9288 (1991).
- <sup>18</sup>C. M. Chen and Y. A. Fwu, *Phys. Rev. E* **63**, 011506 (2000).
- <sup>19</sup>P. J. Flory, *J. Chem. Phys.* **17**, 303 (1949).
- <sup>20</sup>P. G. de Gennes, *Scaling Concepts in Polymer Physics* (Cornell University Press, Ithaka, 1979).
- <sup>21</sup>D. Romeis and M. Lang, *J. Chem. Phys.* **141**, 104902 (2014).
- <sup>22</sup>E. K. Fischer, *Colloidal Dispersions* (Wiley, New York, 1950).
- <sup>23</sup>K. Binder, T. Kreer, and A. Milchev, *Soft Matter* **7**, 7159 (2011).
- <sup>24</sup>H. J. Taunton, C. Toprakcioglu, L. J. Fetters, and J. Klein, *Nature* **332**, 712 (1988).
- <sup>25</sup>J. B. Field, C. Toprakcioglu, R. C. Ball, H. B. Stanley, L. Dai, W. Barford, J. Penfold, G. Smith, and W. Hamilton, *Macromolecules* **25**, 434 (1992).
- <sup>26</sup>M. Ruths, D. Johannsmann, J. Ruhe, and W. Knoll, *Macromolecules* **33**, 3860 (2000).
- <sup>27</sup>T. Drobek, N. D. Spencer, and M. Heuberger, *Macromolecules* **38**, 5254 (2005).
- <sup>28</sup>D. A. Brass and K. R. Shull, *Langmuir* **22**, 9225 (2006).
- <sup>29</sup>S. T. Milner, *Europhys. Lett.* **7**, 695 (1988).
- <sup>30</sup>J. I. Martin and Z. G. Wang, *J. Phys. Chem.* **99**, 2833 (1995).
- <sup>31</sup>T. Kreer and S. M. Balko, *ACS Macro Lett.* **2**, 944 (2013).
- <sup>32</sup>M. Murat and G. Grest, *Phys. Rev. Lett.* **63**, 1074 (1989).
- <sup>33</sup>R. Dickman and P. E. Anderson, *J. Chem. Phys.* **99**, 3112 (1993).
- <sup>34</sup>A. Chakrabarti, P. Nelson, and R. Toral, *J. Chem. Phys.* **100**, 748 (1994).
- <sup>35</sup>F. Lo Verso, L. Yelash, S. A. Egorov, and K. Binder, *J. Chem. Phys.* **135**, 214902 (2011).
- <sup>36</sup>D. J. Mulder and T. L. Kuhl, *Soft Matter* **6**, 5401 (2010).
- <sup>37</sup>J. Z. Wu, *AIChE J.* **52**, 1169 (2006).
- <sup>38</sup>J. Z. Wu and Z. D. Li, *Annu. Rev. Phys. Chem.* **58**, 85 (2007).
- <sup>39</sup>Y. Ye, J. D. McCoy, and J. G. Curro, *J. Chem. Phys.* **119**, 555 (2003).
- <sup>40</sup>T. Jiang, Z. D. Li, and J. Z. Wu, *Macromolecules* **40**, 334 (2007).
- <sup>41</sup>M. Borowko, W. Rzysko, S. Sokolowski, and T. Staszewski, *J. Chem. Phys.* **126**, 214703 (2007).
- <sup>42</sup>T. Jiang and J. Z. Wu, *J. Phys. Chem. B* **112**, 7713 (2008).
- <sup>43</sup>T. Jiang and J. Z. Wu, *J. Chem. Phys.* **129**, 084903 (2008).
- <sup>44</sup>X. F. Xu and D. P. Cao, *J. Chem. Phys.* **130**, 164901 (2009).
- <sup>45</sup>O. Pizio and S. Sokolowski, *Condens. Matter Phys.* **13**, 13602 (2010).
- <sup>46</sup>M. Borowko, S. Sokolowski, and T. Staszewski, *J. Phys. Chem. B* **116**, 3115 (2012).
- <sup>47</sup>Y. L. Xu, X. Q. Chen, X. Han, S. H. Xu, H. L. Liu, and Y. Hu, *Langmuir* **29**, 4988 (2013).
- <sup>48</sup>Y. X. Yu and J. Wu, *J. Chem. Phys.* **117**, 2368 (2002).
- <sup>49</sup>Y. Rosenfeld, *Phys. Rev. Lett.* **63**, 980 (1989).
- <sup>50</sup>M. S. Wertheim, *J. Chem. Phys.* **87**, 7323 (1987).
- <sup>51</sup>Y. X. Yu and J. Z. Wu, *J. Chem. Phys.* **117**, 10156 (2002).
- <sup>52</sup>G. A. Mansoori, N. F. Carnahan, K. E. Starling, and T. W. Leland, *J. Chem. Phys.* **54**, 1523 (1971).
- <sup>53</sup>Y. X. Yu and J. Wu, *J. Chem. Phys.* **116**, 7094 (2002).
- <sup>54</sup>J. P. Hansen and I. R. McDonald, *Theory of Simple Liquids*, 2nd ed. (Academic Press, London, 1990).
- <sup>55</sup>M. Muthukumar and J. S. Ho, *Macromolecules* **22**, 965 (1989).
- <sup>56</sup>R. Toral, A. Chakrabarti, and R. Dickman, *Phys. Rev. E* **50**, 343 (1994).
- <sup>57</sup>F. Shim and M. E. Cates, *J. Phys. (Paris)* **51**, 701 (1990).